

# On the roles of baroclinic modes in eddy-resolving midlatitude ocean dynamics



Igor Shevchenko\*, Pavel Berloff

Department of Mathematics, Imperial College London, Huxley Building, 180 Queen's Gate, London, SW7 2AZ, UK

## ARTICLE INFO

### Article history:

Received 28 May 2016

Revised 27 January 2017

Accepted 6 February 2017

Available online 7 February 2017

### Keywords:

Multi-layer quasi-geostrophic model

Baroclinic modes

Modal energetics

Eddy backscatter

Nonlinear eddy dynamics

Large-scale ocean circulation

## ABSTRACT

This work concerns how different baroclinic modes interact and influence solutions of the midlatitude ocean dynamics described by the eddy-resolving quasi-geostrophic model of wind-driven gyres. We developed multi-modal energetics analysis to illuminate dynamical roles of the vertical modes, carried out a systematic analysis of modal energetics and found that the eddy-resolving dynamics of the eastward jet extension of the western boundary currents, such as the Gulf Stream or Kuroshio, is dominated by the barotropic, and the first and second baroclinic modes, which become more energized with smaller eddy viscosity. In the absence of high baroclinic modes, the energy input from the wind is more efficiently focused onto the lower modes, therefore, the eddy backscatter maintaining the eastward jet and its adjacent recirculation zones is the strongest and overestimated with respect to cases including higher baroclinic modes. In the presence of high baroclinic modes, the eddy backscatter effect on the eastward jet is much weaker. Thus, the higher baroclinic modes play effectively the inhibiting role in the backscatter, which is opposite to what has been previously thought. The higher baroclinic modes are less energetic and have progressively decreasing effect on the flow dynamics; nevertheless, they still play important roles in inter-mode energy transfers (by injecting energy into the region of the most intensive eddy forcing, in the neighborhood of the eastward jet) that have to be taken into account for correct representation of the backscatter and, thus, for determining the eastward jet extension.

© 2017 Elsevier Ltd. All rights reserved.

## 1. Introduction

Dynamics of the large-scale ocean circulation is tackled from various perspectives ranging from theoretical analyses of light process-oriented problems to extremely large computations of comprehensive ocean general circulation models (OGCMs) (e.g., Marsh et al., 2009; Treguier et al., 2014; Gula et al., 2015). In this paper we consider the classical double-gyre QG model in three-, six- and twelve-layer configurations and study the dynamical roles of the vertical baroclinic modes that become available with progressively increasing vertical resolution. Being process-oriented and computationally inexpensive relative to modern OGCMs, the QG model allows one to analyse eddy-resolving flow regimes for a wide range of parameters. In the past, QG studies helped to understand various effects of mesoscale eddies (e.g., Berloff, 2005a; McWilliams, 2008), patterns arising from early bifurcations (e.g., Simonnet et al., 2005; Dijkstra and Ghil, 2005; Sapsis and Dijkstra, 2013), coupling with the atmosphere (e.g., Hogg et al., 2009), and other aspects of flow dynam-

ics. However, the roles of high baroclinic modes (the modes which are higher than the second baroclinic mode) have received little attention and remain poorly understood, both in general and in the specific physical mechanisms affecting the eastward jet extension of the western boundary currents, such as the Gulf Stream or Kuroshio.

A rare study of the influence of horizontal and vertical resolutions on the eastward jet extension is by Barnier et al. (1991), who focused on the eddy-permitting three- and six-layer QG double gyres and concluded that the third and higher baroclinic modes play a *catalytic* role resulting in the nonlinear amplification of the eastward jet. Another series of works (Smith and Vallis, 2001, 2002) studied more idealized, horizontally homogeneous, eddy-resolving QG dynamics and found that, for ocean-like stratification, the kinetic energy is transferred from high baroclinic modes through the first baroclinic mode to the barotropic one. To what extent these energy transfers occur from smaller to larger scales, that is, by the inverse cascade (also known as eddy backscatter) (Vallis, 2006), and affect the eastward jet extension are poorly understood. Although, the impact of the horizontal resolution on the flow dynamics has been extensively studied in QG double gyres (e.g., Shevchenko and Berloff, 2015) and to some extent in com-

\* Corresponding author.

E-mail address: [i.shevchenko@imperial.ac.uk](mailto:i.shevchenko@imperial.ac.uk) (I. Shevchenko).

**Table 1**  
The depths of isopycnal layers (in [m]) for 3L, 6L and 12L models.

Layers	$H_1$	$H_2$	$H_3$	$H_4$	$H_5$	$H_6$	$H_7$	$H_8$	$H_9$	$H_{10}$	$H_{11}$	$H_{12}$
3	0.25	0.75	3.0									
6	0.25	0.25	0.25	0.25	1.00	2.0						
12	0.125	0.125	0.15	0.15	0.15	0.15	0.15	0.2	0.3	0.5	1.0	1.0

prehensive OGCMs (e.g., Kirtman et al., 2012), no studies have attempted to understand the higher vertical baroclinic modes and their influence on the eastward jet in fully eddy-resolving double gyres. The novelty of this work is a systematic study filling this gap in knowledge.

It is well established (e.g., Wunsch (1997)) that ocean circulation is dominated by the barotropic and first baroclinic modal components, but it is also shown that there is significant energy in the higher modes, and the higher is the mode, the less energy it contains. What does this energy do for the lower modes and large-scale flows? Surprisingly little attention has been paid to the dynamical roles of the latter. There is indeed gazing information gap, and the singular exception to it is study by Barnier et al. (1991), which we overhaul and extend. At the moment, we can only assume that just the first few of the higher baroclinic modes do something significant, and the other ones are dynamically inert, because they have too little energy. Our study verifies this assumption in the canonical double-gyre model.

## 2. Double-gyre model

We consider the classical double-gyre QG model, describing idealized midlatitude ocean circulation, in three-, six- and twelve-layer configurations denoted as 3L, 6L and 12L, respectively. The multi-layer QG equations (Pedlosky, 1987; Vallis, 2006) for the potential vorticity (PV) anomaly  $q$  in a domain  $\Omega$  are

$$\partial_t q_i + J(\psi_i, q_i + \beta y) = \delta_{i1} F_w - \delta_{iN} \mu \Delta \psi_i + \nu \Delta^2 \psi_i, \quad 1 \leq i \leq N, \quad (1)$$

where  $J(f, g) \equiv f_x g_y - f_y g_x$ , and  $\delta_{ij}$  is the Kronecker symbol;  $N = \{3, 6, 12\}$  is the corresponding number of stacked isopycnal fluid layers with depths given in Table 1, and with both density and index increasing downward. The computational domain  $\Omega$  is a square, closed, flat-bottom basin of dimensions  $L \times L \times 4$  km, with  $L = 3840$  km. The asymmetric wind curl is the only forcing (i.e., Ekman pumping) that drives the double-gyre ocean circulation, and it is given by

$$F_w = \begin{cases} -1.80 \pi \tau_0 \sin(\pi y / y_0), & y \in [0, y_0], \\ 2.22 \pi \tau_0 \sin(\pi(y - y_0) / (L - y_0)), & y \in [y_0, L], \end{cases}$$

with a wind stress  $\tau_0 = 0.3 \text{ N m}^{-2}$  and the tilted zero forcing line  $y_0 = 0.4L + 0.2x$ ,  $x \in [0, L]$ , used to avoid the symmetric solution (Berloff and McWilliams, 1999a; Berloff et al., 2007). In order for the 12L model to be consistent with the 3L and 6L case, the wind forcing is applied to the first two layers, since  $H_1^{(12)} = H_2^{(12)} = 0.5H_1^{(6)}$ , where the superscript indicates the number of the model. The planetary vorticity gradient is  $\beta = 2 \times 10^{-11} \text{ m}^{-1} \text{ s}^{-1}$ , the bottom friction parameter is  $\mu = 4 \times 10^{-8} \text{ s}^{-1}$  and the lateral eddy viscosity  $\nu$  is a variable parameter specified further below.

The layerwise PV anomaly  $q_i$  and the velocity streamfunction  $\psi_i$  are dynamically coupled through the system of elliptic equations:

$$q_i = \Delta \psi_i - (1 - \delta_{i1}) S_{i1} (\psi_i - \psi_{i-1}) - (1 - \delta_{iN}) S_{i2} (\psi_i - \psi_{i+1}), \quad 1 \leq i \leq N, \quad (2)$$

with the stratification parameters  $S_{i1}$ ,  $S_{i2}$  (Section 5.3.2 in Vallis (2006)) chosen so that to make Rossby deformation radii as similar

as possible between the models (Table 2). Note that for consistency the first Rossby radius ( $Rd_1 = 40$  km) is the same across all model stratifications. System (1)–(2) is augmented with the integral mass conservation constraints (McWilliams, 1977):

$$\partial_t \iint_{\Omega} (\psi_i - \psi_{i+1}) dy dx = 0, \quad 1 \leq i \leq N - 1, \quad (3)$$

with the zero initial condition, and with the partial-slip lateral boundary condition:

$$\partial_{\mathbf{nn}} \psi_i - \alpha^{-1} \partial_{\mathbf{n}} \psi_i = 0, \quad 1 \leq i \leq N, \quad (4)$$

where  $\alpha = 120$  km (Berloff and McWilliams, 1999b) and  $\mathbf{n}$  is the normal-to-wall and facing inward unit vector. This condition, which is a simple parameterization of dynamically unresolved near-boundary processes, prescribes the tangential velocity component in terms of the exponential decay law based on the characteristic boundary layer thickness  $\alpha$ . Along with the boundary condition (4) we ensure no normal flow condition on  $\psi_i$ ,  $1 \leq i \leq N$ .

The QG model (1)–(4) is solved on the appropriate grid with the high-resolution CABARET method based on a second-order, non-dissipative and low-dispersive conservative advection scheme (Karabasov et al., 2009). The distinctive feature of this method is its ability to simulate large-Reynolds flow regimes cost-efficiently.

The model is initially spun up from the state of rest over the time interval  $T_{\text{spin}}$  (about 20 years), which depends on the eddy viscosity  $\nu$  and vertical resolution  $N$ , until the solution becomes statistically equilibrated, as indicated by the total energy time series. Then, the solution is computed for another  $T_{\text{sim}} = 40$  years and analyzed. To guarantee converged solutions for the eddy viscosities  $\nu = \{50, 100\} \text{ m}^2 \text{ s}^{-1}$ , which are considered in the paper, all our numerical experiments were carried out on the appropriate uniform horizontal grids  $G = \{257^2, 513^2\}$ , where the grid size  $X \times X$  is indicated as  $X^2$ . We assume that the solution is converged if the  $l^2$ -norm relative difference  $\delta(f, g) = \|g - f\|_2 / \|f\|_2$  between a coarse- and fine-grid solutions  $g$  and  $f$  is sufficiently small (less than 5%). We also use the relative error  $\delta$  to compare different solutions and their characteristics. More details on the solution convergence at these and much smaller values of  $\nu$  can be found in Shevchenko and Berloff (2015).

Note that the horizontal resolution in the analyzed solutions may look insufficient, but we have performed a formal numerical convergence study to make sure that all dynamically important scales in the model and flow regime considered are resolved. In confirmation of this we have compared  $257^2$  and  $513^2$  solutions for  $\nu = 100 \text{ m}^2 \text{ s}^{-1}$  in 3L and 6L cases, and found a less than 5% difference between the coarse and refined time-mean solutions, as well as between the corresponding energy diagrams, although the latter show a less than 10% difference, since using flow energetics as a metric of convergence assumes higher resolution for the solution to be converged. This result disregards the importance of resolving the smallest length scales in the considered ocean model and flow regime. Other flow regimes, such as those dominated by surface QG dynamics may exhibit much stronger dependence on finer grid resolution, but this is apparently not our case, which focuses on the dynamics of the main pycnocline. In our case horizontal eddy scales are dominated by the deformation scales of the lowest vertical modes.

**Table 2**

The Rossby deformation radii (in [km]) for 3L, 6L and 12L models.

Layers	Rd <sub>1</sub>	Rd <sub>2</sub>	Rd <sub>3</sub>	Rd <sub>4</sub>	Rd <sub>5</sub>	Rd <sub>6</sub>	Rd <sub>7</sub>	Rd <sub>8</sub>	Rd <sub>9</sub>	Rd <sub>10</sub>	Rd <sub>11</sub>
3	40.0	23.0									
6	40.0	16.0	11.6	9.8	7.8						
12	40.0	15.7	10.7	8.2	6.6	6.2	5.3	4.6	3.9	3.6	3.2

### 3. Analyses of the double-gyre solutions

In this section we study effects of vertical modes in 3L, 6L and 12L solutions. As the starting point, we decompose each flow field into its time-mean and fluctuating components, denoted by an overbar and a prime, respectively, and derive the energy balance equations for the QG model (1)–(4) in the layer- and mode-wise formulations. To make the derivation clearer to the reader and to avoid unnecessary complications, we will write the derivation for the 3L model followed by its modewise analogue; the derivation for the 6L and 12L cases follows the same lines.

#### Isopycnal layers

The layerwise energy equations can be obtained by multiplying (1) by a vector  $-\boldsymbol{\psi} = -(\psi_1, \psi_2, \psi_3)^T$  and recasting the result in the following form

$$\begin{aligned} -\psi_1 \frac{\partial q_1}{\partial t} - \psi_1 J_1 &= -\psi_1 F_w - \psi_1 \nu \Delta^2 \psi_1, \\ -\psi_2 \frac{\partial q_2}{\partial t} - \psi_2 J_2 &= -\psi_2 \nu \Delta^2 \psi_2, \\ -\psi_3 \frac{\partial q_3}{\partial t} - \psi_3 J_3 &= \psi_3 \mu \Delta \psi_3 - \psi_3 \nu \Delta^2 \psi_3, \end{aligned} \quad (5)$$

where  $J_i = J(\psi_i, q_i + \beta y)$ .

Using the identity

$$\frac{1}{2} \frac{\partial}{\partial t} (\nabla \chi)^2 = \nabla \cdot \chi \nabla \left( \frac{\partial \chi}{\partial t} \right) - \chi \Delta \left( \frac{\partial \chi}{\partial t} \right) \quad (6)$$

and substituting (2) into (5) leads to

$$\begin{aligned} \frac{1}{2} \frac{\partial}{\partial t} ((\nabla \psi_1)^2 + S_{12} \psi_1^2) & - \nabla \cdot \mathbf{T}_1 = -\psi_1 F_w - \psi_1 \nu \Delta^2 \psi_1 + \psi_1 S_{12} \frac{\partial \psi_2}{\partial t}, \\ \frac{1}{2} \frac{\partial}{\partial t} ((\nabla \psi_2)^2 + (S_{21} + S_{22}) \psi_2^2) & - \nabla \cdot \mathbf{T}_2 = -\psi_2 \nu \Delta^2 \psi_2 + \psi_2 \left( S_{21} \frac{\partial \psi_1}{\partial t} + S_{22} \frac{\partial \psi_3}{\partial t} \right), \\ \frac{1}{2} \frac{\partial}{\partial t} ((\nabla \psi_3)^2 + S_{31} \psi_3^2) & - \nabla \cdot \mathbf{T}_3 = \psi_3 \mu \Delta \psi_3 - \psi_3 \nu \Delta^2 \psi_3 + \psi_3 S_{31} \frac{\partial \psi_2}{\partial t}, \end{aligned} \quad (7)$$

with the energy flux vector

$$\mathbf{T}_i = \frac{\psi_i^2}{2} \left( \frac{\partial q_i}{\partial y} + \beta, -\frac{\partial q_i}{\partial x} \right) + \psi_i \nabla \left( \frac{\partial \psi_i}{\partial t} \right), \quad 1 \leq i \leq 3.$$

By applying the vector identities

$$\begin{aligned} \psi \Delta \psi &= \nabla \cdot (\psi \nabla \psi) - (\nabla \psi)^2, \\ \psi \Delta^2 \psi &= \nabla \cdot (\psi \nabla (\Delta \psi) - \Delta \psi \nabla \psi) + (\Delta \psi)^2 \end{aligned}$$

we split the term  $\psi_i \Delta^2 \psi_i$  on the right hand side of (7) into the tendency term and divergent parts:

$$\begin{aligned} \frac{1}{2} \frac{\partial}{\partial t} ((\nabla \psi_1)^2 + S_{12} \psi_1^2) & - \nabla \cdot \mathbf{B}_1 = F_1 + \psi_1 S_{12} \frac{\partial \psi_2}{\partial t}, \\ \frac{1}{2} \frac{\partial}{\partial t} ((\nabla \psi_2)^2 + (S_{21} + S_{22}) \psi_2^2) & - \nabla \cdot \mathbf{B}_2 = F_2 + \psi_2 \left( S_{21} \frac{\partial \psi_1}{\partial t} + S_{22} \frac{\partial \psi_3}{\partial t} \right), \\ \frac{1}{2} \frac{\partial}{\partial t} ((\nabla \psi_3)^2 + S_{31} \psi_3^2) & - \nabla \cdot \mathbf{B}_3 = F_3 + \psi_3 S_{31} \frac{\partial \psi_2}{\partial t}, \end{aligned} \quad (8)$$

where

$$S_{21} = \frac{H_1}{H_2} S_{12}, \quad S_{22} = \frac{H_1}{H_2} \gamma S_{12}, \quad S_{31} = \frac{H_1}{H_3} \gamma S_{12}, \quad \gamma = \frac{S_{22}}{S_{21}},$$

and

$$\begin{aligned} \mathbf{B}_i &= \frac{\psi_i^2}{2} \left( \frac{\partial q_i}{\partial y} + \beta, -\frac{\partial q_i}{\partial x} \right) + \psi_i \nabla \left( \frac{\partial \psi_i}{\partial t} \right) \\ & - \nu (\psi_i \nabla (\Delta \psi_i) - \Delta \psi_i \nabla \psi_i) + \delta_{3i} \mu (\psi_i \nabla \psi_i), \quad 1 \leq i \leq 3, \end{aligned}$$

with

$$F_i = \begin{cases} F_w - D_{1,v} & \text{for } i = 1, \\ -D_{2,v} & \text{for } i = 2, \\ -D_{\mu} - D_{3,v} & \text{for } i = 3, \end{cases}$$

and

$$F_w = -\psi_1 F_w, \quad D_{i,v} = \nu (\Delta \psi_i)^2, \quad D_{\mu} = \mu (\nabla \psi_3)^2.$$

In order to obtain the available potential energy, the last term on the right hand side of each equation in (8) has to be brought under the time derivative on the left hand side. To this end, we multiply the  $i$ -th equation (8) by  $H_i/H$  and write it as

$$\frac{\partial E_i}{\partial t} - \frac{H_i}{H} \nabla \cdot \mathbf{B}_i = \frac{H_i}{H} F_i, \quad 1 \leq i \leq 3, \quad (9)$$

with

$$E_i = K_i + APE_i,$$

where the kinetic energy of the  $i$ -th layer is  $K_i = \frac{1}{2} \frac{H_i}{H} (\nabla \psi_i)^2$ , and the available potential energy  $APE_i$  is distributed vertically as

$$APE_i = \begin{cases} \frac{H_1}{H} \frac{S_{12}}{4} [\psi]_{12}^2 & \text{for } i = 1, \\ \frac{H_1}{H} \frac{S_{12}}{4} ([\psi]_{21}^2 + \gamma [\psi]_{23}^2) & \text{for } i = 2, \\ \frac{H_1}{H} \frac{S_{12}}{4} \gamma [\psi]_{32}^2 & \text{for } i = 3, \end{cases}$$

with  $H = \sum_{i=1}^3 H_i$  and  $[\psi]_{ij} = \psi_i - \psi_j$ .

To proceed, we define the total basin-average time-mean  $\bar{K}_i$  and  $\bar{APE}_i$  of the flow as follows

$$\bar{K}_i = \frac{1}{2} \frac{H_i}{HA} \iint_{\Omega} \overline{(\nabla \psi_i)^2} dx dy,$$

and

$$\overline{APE}_i = \begin{cases} \frac{1}{4} \frac{H_1}{HA} \iint_{\Omega} \frac{H_1}{H} \frac{S_{12}}{4} \overline{[\psi]_{12}^2} dx dy & \text{for } i = 1, \\ \frac{1}{4} \frac{H_1}{HA} \iint_{\Omega} \frac{H_1}{H} \frac{S_{12}}{4} \overline{([\psi]_{21}^2 + \gamma[\psi]_{23}^2)} dx dy & \text{for } i = 2, \\ \frac{1}{4} \frac{H_1}{HA} \iint_{\Omega} \frac{H_1}{H} \frac{S_{12}}{4} \overline{\gamma[\psi]_{32}^2} dx dy & \text{for } i = 3, \end{cases}$$

where  $A = L_x L_y H$ .

We also define the time-mean kinetic energy of eddies  $\overline{K}_i'$  as

$$\overline{K}_i' = \frac{1}{2} \frac{H_i}{HA} \iint_{\Omega} \overline{(\nabla \psi_i')^2} dx dy, \quad 1 \leq i \leq 3,$$

and the time-mean available potential energy of eddies  $\overline{APE}'$  as

$$\overline{APE}'_i = \begin{cases} \frac{1}{4} \frac{H_1}{HA} \iint_{\Omega} \frac{H_1}{H} \frac{S_{12}}{4} \overline{[\psi']_{12}^2} dx dy & \text{for } i = 1, \\ \frac{1}{4} \frac{H_1}{HA} \iint_{\Omega} \frac{H_1}{H} \frac{S_{12}}{4} \overline{([\psi']_{21}^2 + \gamma[\psi']_{23}^2)} dx dy & \text{for } i = 2, \\ \frac{1}{4} \frac{H_1}{HA} \iint_{\Omega} \frac{H_1}{H} \frac{S_{12}}{4} \overline{\gamma[\psi']_{32}^2} dx dy & \text{for } i = 3. \end{cases}$$

Thus, the mean-flow energy on the  $i$ -th layer  $\langle E_i \rangle$  is given by

$$\langle E_i \rangle = \overline{E}_i - \overline{E}_i', \quad 1 \leq i \leq 3.$$

In order to study how the energy is transferred between the layers, we extracted the energy transfer terms  $C_{ij}$  from the divergence operator in system (9), and after further manipulations obtained

$$\begin{aligned} \frac{\partial E_1}{\partial t} - \nabla \cdot \left( \frac{H_1}{H} \mathbf{G}_1 + \frac{H_1}{H} \mathbf{C}_1 \right) &= \frac{H_1}{H} F_1 + C_{12}, \\ \frac{\partial E_2}{\partial t} - \nabla \cdot \left( \frac{H_2}{H} \mathbf{G}_2 + \frac{H_1}{H} \mathbf{C}_2 \right) &= \frac{H_2}{H} F_2 - C_{12} + C_{23}, \\ \frac{\partial E_3}{\partial t} - \nabla \cdot \left( \frac{H_3}{H} \mathbf{G}_3 + \frac{H_1}{H} \mathbf{C}_3 \right) &= \frac{H_3}{H} F_3 - C_{23}, \end{aligned} \quad (10)$$

with

$$\begin{aligned} \mathbf{G}_i &= \frac{\psi_i^2}{2} \left( \frac{\partial}{\partial y} \Delta \psi_i + \beta, -\frac{\partial}{\partial x} \Delta \psi_i \right) + \psi_i \nabla \left( \frac{\partial \psi_i}{\partial t} \right) \\ &\quad - \nu (\psi_i \nabla (\Delta \psi_i) - \Delta \psi_i \nabla \psi_i) + \delta_{3i} \mu (\psi_i \nabla \psi_i), \quad 1 \leq i \leq 3, \end{aligned} \quad (11)$$

and

$$\begin{aligned} \mathbf{C}_i &= \frac{S_{12}}{4} (1 - \delta_{3i}) \left( \psi_i^2 \frac{\partial \psi_{i+1}}{\partial y} + \psi_{i+1}^2 \frac{\partial \psi_i}{\partial y}, -\psi_i^2 \frac{\partial \psi_{i+1}}{\partial x} - \psi_{i+1}^2 \frac{\partial \psi_i}{\partial x} \right) \\ &\quad + \gamma \frac{S_{12}}{4} (1 - \delta_{1i}) \left( \psi_{i-1}^2 \frac{\partial \psi_i}{\partial y} + \psi_i^2 \frac{\partial \psi_{i-1}}{\partial y}, \right. \\ &\quad \left. -\psi_{i-1}^2 \frac{\partial \psi_i}{\partial x} - \psi_i^2 \frac{\partial \psi_{i-1}}{\partial x} \right), \quad 1 \leq i \leq 3, \end{aligned} \quad (12)$$

where the terms  $C_{ij}$  (responsible for the energy transfer between the  $i$ -th and  $j$ -th layers) are

$$\begin{aligned} C_{12} &= \frac{H_1}{H} \frac{S_{12}}{2} J(\psi_1, \psi_2)(\psi_1 + \psi_2), \\ C_{23} &= \gamma \frac{H_1}{H} \frac{S_{12}}{2} J(\psi_2, \psi_3)(\psi_2 + \psi_3). \end{aligned}$$

Next, we time averaged equations (10), integrated them over the basin  $\Omega$ , and applied the Gauss–Ostrogradsky theorem:

$$\begin{aligned} -\frac{H_1}{H} \oint_{\Gamma} \overline{\mathbf{G}}_1 \cdot \mathbf{n} d\Gamma &= \langle \overline{F}_w \rangle - \langle \overline{D}_{1,v} \rangle + \langle \overline{C}_{12} \rangle, \\ -\frac{H_2}{H} \oint_{\Gamma} \overline{\mathbf{G}}_2 \cdot \mathbf{n} d\Gamma &= -\langle \overline{D}_{2,v} \rangle - \langle \overline{C}_{12} \rangle + \langle \overline{C}_{23} \rangle, \\ -\frac{H_3}{H} \oint_{\Gamma} \overline{\mathbf{G}}_3 \cdot \mathbf{n} d\Gamma &= -\langle \overline{D}_{\mu} \rangle - \langle \overline{D}_{3,v} \rangle - \langle \overline{C}_{23} \rangle, \end{aligned} \quad (13)$$

where  $\langle \overline{F}_w \rangle$  is the basin-average wind forcing  $F_w$ ,  $\langle \overline{C}_{ij} \rangle$  is the energy transfer rate between the layers,  $\langle \overline{D}_{1,v} \rangle$  and  $\langle \overline{D}_{\mu} \rangle$  are the energy dissipation due to the eddy viscosity and bottom friction, respectively. Here, the overbar and the angle brackets denote the time and basin averages, respectively.

As it follows from the boundary condition (4), the total flux across the boundary  $\Gamma$  in equation (13) does not vanish and becomes

$$\begin{aligned} \mathcal{I}_{\Gamma,i} &\equiv -\frac{H_i}{H} \oint_{\Gamma} \overline{\mathbf{G}}_i \cdot \mathbf{n} d\Gamma = -\frac{H_i}{H} \oint_{\Gamma} \left[ \left( \frac{\psi_i^2}{2} \frac{\partial \omega_i}{\partial y}, -\frac{\psi_i^2}{2} \frac{\partial \omega_i}{\partial x} \right) \cdot \mathbf{n} \right. \\ &\quad \left. + \alpha \psi_i \frac{\partial \widehat{\omega}_i}{\partial t} - \nu \left( \psi_i \frac{\partial \omega_i}{\partial \mathbf{n}} - \alpha \widehat{\omega}_i \widehat{\omega}_i \right) + \delta_{3i} \mu \alpha \overline{\psi_i \widehat{\omega}_i} \right] d\Gamma, \end{aligned} \quad (14)$$

where  $\omega_i = \Delta \psi_i$ ,  $\widehat{\omega}_i = \partial_{\mathbf{nn}} \psi_i$ . We decompose  $\mathcal{I}_{\Gamma,i} = \mathcal{I}_{\Gamma,i}^+ + \mathcal{I}_{\Gamma,i}^-$ , relocate it to the right hand side of (13) and treat it, depending on the sign, as the forcing  $\mathcal{I}_{\Gamma,i}^+$  or dissipation  $\mathcal{I}_{\Gamma,i}^-$ . Thus, the layerwise energy balance equations become

$$\begin{aligned} 0 &= \langle \overline{F}_1 \rangle - \langle \overline{D}_1 \rangle + \langle \overline{C}_{12} \rangle, \\ 0 &= \langle \overline{F}_2 \rangle - \langle \overline{D}_2 \rangle - \langle \overline{C}_{12} \rangle + \langle \overline{C}_{23} \rangle, \\ 0 &= \langle \overline{F}_3 \rangle - \langle \overline{D}_3 \rangle - \langle \overline{C}_{23} \rangle, \end{aligned} \quad (15)$$

where  $\langle \overline{F}_i \rangle = \delta_{1i} \langle \overline{F}_w \rangle + \mathcal{I}_{\Gamma,i}^+$ ,  $\langle \overline{D}_i \rangle = -\delta_{3i} \langle \overline{D}_{\mu} \rangle - \langle \overline{D}_{i,v} \rangle + \mathcal{I}_{\Gamma,i}^-$ ,  $1 \leq i \leq 3$ .

*Vertical modes*

In order to express the QG equations (1) in terms of the vertical modes  $\phi$  we make use of the stratification matrix

$$\mathbf{S} = \begin{pmatrix} S_{12} & -S_{12} & 0 \\ -S_{21} & S_{21} + S_{22} & -S_{22} \\ 0 & -S_{31} & S_{31} \end{pmatrix}$$

and rewrite the system of elliptic equations (2) in the vector form as

$$\mathbf{q} = \Delta \boldsymbol{\psi} - \mathbf{S} \boldsymbol{\psi}. \quad (16)$$

Multiplying (16) by some matrix  $\Theta$  yields

$$\Theta \mathbf{q} = \Delta \Theta \boldsymbol{\psi} - \Theta \mathbf{S} \boldsymbol{\psi}. \quad (17)$$

The matrix  $\Theta$  is chosen so that  $\Lambda = \Theta \mathbf{S} \Theta^{-1}$ , where  $\Lambda$  is the diagonal matrix of the eigenvalues of the stratification matrix  $\mathbf{S}$ , and columns of  $\Theta^{-1}$  are the corresponding eigenvectors of  $\mathbf{S}$ . Hence, equation (17) can be rewritten as

$$\Theta \mathbf{q} = \Delta \Theta \boldsymbol{\psi} - \Lambda \Theta \boldsymbol{\psi}. \quad (18)$$

Thus, the QG equations (1) can be projected from layers onto modes by the linear transformation  $\Theta$ :  $\boldsymbol{\psi} \rightarrow \boldsymbol{\phi}$ , where  $\boldsymbol{\phi} = (\phi_0, \phi_1, \phi_2)$ ,  $\phi_0$  is the barotropic mode, and  $\phi_1, \phi_2$  are the first and second baroclinic modes. The inverse transformation is given by  $\Theta^{-1}$ :  $\boldsymbol{\phi} \rightarrow \boldsymbol{\psi}$ . To keep the notations consistent with the definition of the modes we enumerated the entries  $\theta_{ij}$  and  $\tilde{\theta}_{ij}$  of the matrices  $\Theta$  and  $\Theta^{-1}$  from 0 to  $N-1$ .

Substitution of (16) into (1) and subsequent multiplication of the  $i$ -th equation in (1) by  $\theta_{ji}$  lead to

$$\begin{aligned} \theta_{j1} \left( \Delta \left( \frac{\partial \psi_1}{\partial t} \right) - S_{12} \left( \frac{\partial \psi_1}{\partial t} - \frac{\partial \psi_2}{\partial t} \right) + J_{11} \right) &= \theta_{j1} (F_w + \nu \Delta^2 \psi_1), \\ \theta_{j2} \left( \Delta \left( \frac{\partial \psi_2}{\partial t} \right) - S_{21} \left( \frac{\partial \psi_2}{\partial t} - \frac{\partial \psi_1}{\partial t} \right) \right. \\ &\quad \left. - S_{22} \left( \frac{\partial \psi_2}{\partial t} - \frac{\partial \psi_3}{\partial t} \right) + J_{22} \right) = \theta_{j2} \nu \Delta^2 \psi_2, \end{aligned}$$

$$\begin{aligned} & \theta_{j3} \left( \Delta \left( \frac{\partial \psi_3}{\partial t} \right) - S_{31} \left( \frac{\partial \psi_3}{\partial t} - \frac{\partial \psi_2}{\partial t} \right) + J_{33} \right) \\ & = \theta_{j3} (v \Delta^2 \psi_3 - \mu \Delta \psi_3), \end{aligned} \quad (19)$$

where  $1 \leq j \leq 3$  and  $J_{ii} = J(\psi_i, q_i)$ .

Summing up equations (19) and taking into account (18) gives the following equations for the vertical modes:

$$\begin{aligned} & \Delta \left( \frac{\partial \phi_m}{\partial t} \right) - \lambda_m \frac{\partial \phi_m}{\partial t} + \sum_{i=1}^3 \theta_{mi} J_{ii} \\ & = \theta_{m1} F_w - \theta_{m3} \mu \Delta \psi_3 + v \Delta^2 \phi_m, \quad 0 \leq m \leq 2, \end{aligned} \quad (20)$$

where  $\lambda_m$  is the  $m$ -th eigenvalue of the matrix  $\Lambda$ .

The modewise energy equations can be derived similarly to their layerwise analogues (15) by multiplying the  $m$ -th equation (20) by  $-\phi_m$  to have

$$\begin{aligned} & \frac{1}{2} \frac{\partial \tilde{E}_m}{\partial t} - \nabla \cdot \tilde{\mathbf{G}}_m - \phi_m \sum_{i=1}^3 \theta_{mi} \tilde{J}_{i,2,2} \\ & = \tilde{F}_{m,w} - \tilde{D}_{m,\mu} - \tilde{D}_{m,v}, \quad 0 \leq m \leq 2, \end{aligned} \quad (21)$$

where a tilde represents modal values, and the modal energies are given by

$$\tilde{E}_m = \tilde{K}_m + \tilde{P}_m, \quad \tilde{K}_m = (\nabla \phi_m)^2, \quad \tilde{P}_m = \lambda_m \phi_m^2,$$

and the modal form of the energy flux given by

$$\begin{aligned} \tilde{\mathbf{G}}_m &= \left( \frac{\beta}{2} \phi_m^2, 1 \right) + \phi_m \nabla \left( \frac{\partial \phi_m}{\partial t} \right) - v (\phi_m \nabla (\Delta \phi_m) - \Delta \phi_m \nabla \phi_m) \\ &+ \theta_{m3} \tilde{\theta}_{3m} \mu (\phi_m \nabla \phi_m). \end{aligned} \quad (22)$$

The modal representation of the Jacobian  $\tilde{J}_{i,k_1,l_1}$  in (21) is

$$\tilde{J}_{i,k',l'} = \sum_{k=0}^{k_1} \sum_{l=0}^{l_1} J(\tilde{\theta}_{ik} \phi_k, \tilde{\theta}_{il} \xi_l), \quad (23)$$

where  $\xi$  is the modal PV anomaly. The modal forcing and dissipation in (21) are given by

$$\begin{aligned} \tilde{F}_{m,w} &= -\theta_{m1} \phi_m F_w, \quad \tilde{D}_{m,\mu} = \theta_{m3} \mu \sum_{i=1}^3 \tilde{\theta}_{3i} \nabla \phi_i \cdot \nabla \phi_m, \\ \tilde{D}_{m,v} &= v (\Delta \phi_m)^2. \end{aligned}$$

As in the layerwise case, we average (21) in time and space, and apply the Gauss–Ostrogradsky theorem resulting in

$$\begin{aligned} & - \oint_{\Gamma} \tilde{\mathbf{G}}_m \cdot \mathbf{n} - \langle \tilde{\mathbf{C}}_{mp} \rangle \\ & = \langle \tilde{F}_{m,w} \rangle - \langle \tilde{D}_{m,\mu} \rangle - \langle \tilde{D}_{m,v} \rangle \quad 0 \leq m \leq 2, \quad p = 0, 1, 2, \end{aligned} \quad (24)$$

with the energy transfer terms between the  $m$ -th and  $p$ -th modes given by

$$\langle \tilde{\mathbf{C}}_{mp} \rangle = \left\langle \phi_m \sum_{i=1}^3 \theta_{mi} \tilde{J}_{i,k_1,l_1} \right\rangle, \quad k_1 = l_1 = \{m, p\}.$$

We denote the boundary integral in (24) by  $\tilde{\mathcal{I}}_{\Gamma,m}$  and decompose it into the sum of the forcing  $\tilde{\mathcal{I}}_{\Gamma,m}^+$  and dissipative  $\tilde{\mathcal{I}}_{\Gamma,m}^-$  terms, as in the layerwise case. Thus, the modewise energy balance equations become

$$\begin{aligned} 0 &= \langle \tilde{F}_m \rangle - \langle \tilde{D}_m \rangle + \langle \tilde{\mathbf{C}}_{01} \rangle + \langle \tilde{\mathbf{C}}_{02} \rangle, \\ 0 &= \langle \tilde{F}_m \rangle - \langle \tilde{D}_m \rangle + \langle \tilde{\mathbf{C}}_{10} \rangle + \langle \tilde{\mathbf{C}}_{12} \rangle, \\ 0 &= \langle \tilde{F}_m \rangle - \langle \tilde{D}_m \rangle + \langle \tilde{\mathbf{C}}_{20} \rangle + \langle \tilde{\mathbf{C}}_{21} \rangle, \end{aligned} \quad (25)$$

where  $\langle \tilde{F}_m \rangle = \langle \tilde{F}_{m,w} \rangle + \tilde{\mathcal{I}}_{\Gamma,m}^+$ ,  $\langle \tilde{D}_m \rangle = \langle \tilde{D}_{m,\mu} \rangle + \langle \tilde{D}_{m,v} \rangle + \tilde{\mathcal{I}}_{\Gamma,m}^-$ .

From the modewise energy balance equations (25), we computed the energy transfers between the modes, as well as the energies of the time-mean flow ( $\tilde{E}$ ) and the fluctuating ( $\tilde{E}'$ ) component of the mode. The formalism was extended to the 6L and 12L models, and used to estimate how the difference between 3L, 6L and 12L solutions is reflected in the modal energetics.

### Modal energetics

Here we study how the decreasing eddy viscosity  $\nu$  influences the flow dynamics. In particular, we analyze the penetration length of the eastward jet  $L_p$  (defined as the distance from the western boundary to the most eastern point at the tip of the time-mean jet, where the time-mean flow speed is less than  $0.1 \text{ m s}^{-1}$ ), the volume transport  $Q$  (the difference between the maximum and minimum of the time-mean barotropic transport streamfunction given in [Sv]), and the relative  $l^2$ -norm difference  $\delta$  between two fields.

As seen in Fig. 1, the smaller is  $\nu$ , the stronger is the eastward jet extension and the larger is  $Q$  (Table 3); also,  $L_p$  and  $Q$  are in general larger with fewer layers and smaller  $\nu$ , although there might be some small exceptions. The global relative difference between 3L and 6L solutions is  $\delta(\overline{\psi}_1^{(3)}, \overline{\psi}_1^{(6)}) = 0.61$  and the analogous local difference reaches its maximum in the eastward jet region. However, the 6L and 12L solutions are similar, and  $\delta(\overline{\psi}_1^{(6)}, \overline{\psi}_1^{(12)}) = 0.05$ .

The discrepancy between 3L and 6L solutions is due to the differing vertical resolution, but such an explanation misses the underlying physical mechanism which involves higher baroclinic modes. To address this issue we studied more thoroughly the solutions with  $\nu = 100 \text{ m}^2 \text{ s}^{-1}$ , while leaving out (due to the lack of computational resources) similarly detailed analyses of the problem with  $\nu = 50 \text{ m}^2 \text{ s}^{-1}$ . However, on the basis of qualitative comparison of the 3L and 6L solutions in Shevchenko and Berloff (2015) and our present analysis, we argue that the dynamics at  $\nu = 50 \text{ m}^2 \text{ s}^{-1}$  is qualitatively similar, though more energetic. Thus, we treat the dynamics at  $\nu = 100 \text{ m}^2 \text{ s}^{-1}$  as the reference one.

We use the modewise energy balance equations (25) to study how the difference between 3L and 6L solutions is reflected in the modal energetics. The modewise energy diagrams for the 3L and 6L solutions (Figs. 2 and 3) show that in all solutions the main energy transfers are between the barotropic, first and second baroclinic modes, and in the 6L solution both the energy of the time-mean flow and the energies of the fluctuating components of these modes are larger. Note that all energy terms in the energy diagrams are non-dimensional and normalized to the total layerwise energy (the total energy integrated over all the layers); the velocity is defined in units  $u_s = \text{cm s}^{-1}$ , the length scale is  $l_s = L/(\sqrt{G} - 1)$  (the grid interval) and the time scale  $t_s = l_s/u_s$ . As one can see in (Figs. 2 and 3, the energy of fluctuations is concentrated in the lower modes  $\phi_0, \phi_1, \phi_2$ . Moreover, the energy exchanges between these modes dominate and make the barotropic, first and second baroclinic modes players of fundamental importance in determining the eastward jet extension. To support this conclusion further, we amplified each mode with extra forcing and observed the resulting amplifications of the eastward jet. For this we introduced the modewise forcing anomaly

$$\tilde{F} = \Theta^{-1}(\tilde{\mathbf{f}} \odot F),$$

in which  $\tilde{\mathbf{f}} = (\tilde{f}_0, \tilde{f}_1, \tilde{f}_2)^T$  and the symbol  $\odot$  denotes a component-wise multiplication, namely  $\tilde{\mathbf{f}} \odot F = (\tilde{f}_0 F_0, \tilde{f}_1 F_1, \tilde{f}_2 F_2)$ , where  $F_i$  is the projection of the wind forcing  $F_w$  onto the  $i$ -th mode. For the spatial pattern of  $F$  it is natural to take the wind forcing  $F_w$ , since it affects all the modes and does not project on the eastward jet, although other choices can be also justified. Thus, the modewise

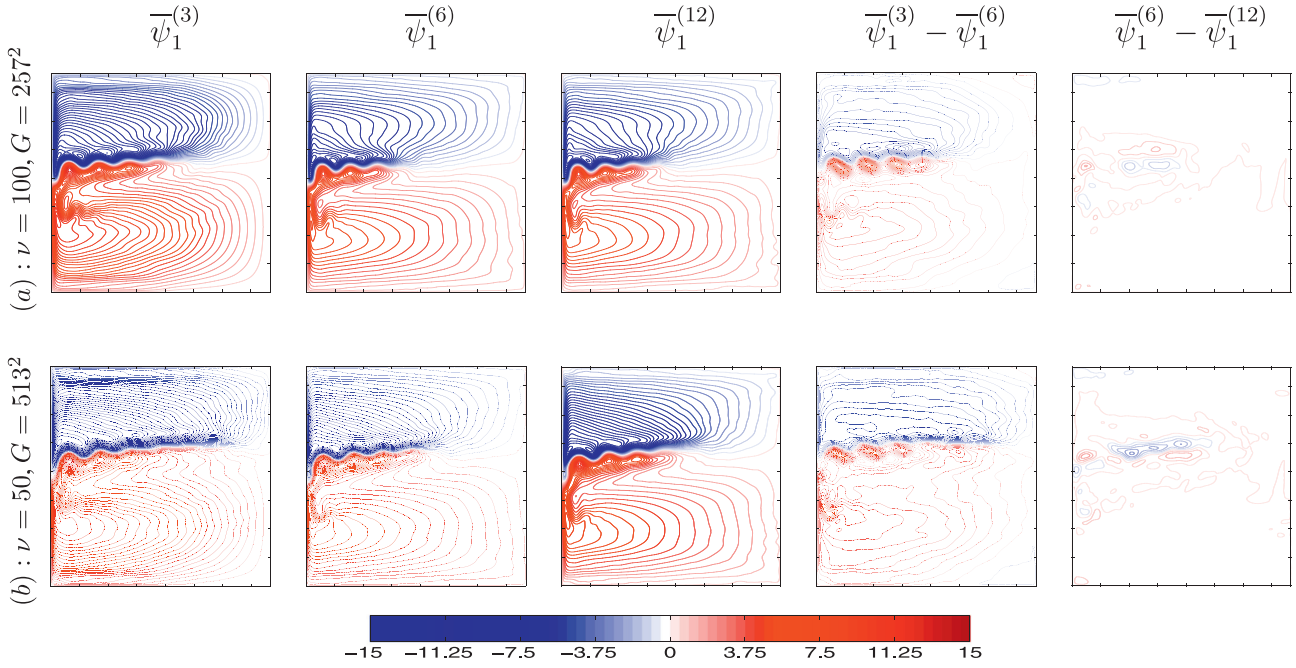


**Fig. 1.** A sequence of time-mean solutions for decreasing eddy viscosity  $\nu$ . The time-mean transport velocity streamfunction  $\bar{\psi}_1$  for different models, grids  $G$  and viscosities  $\nu$  [ $\text{m}^2 \text{s}^{-1}$ ]; contour interval is 0.5 Sv. Note that  $L_p^{(3)} > L_p^{(6)}$ , but  $L_p^{(6)} \approx L_p^{(12)}$  for  $\nu = \{50, 100\} \text{ m}^2 \text{ s}^{-1}$ .

**Table 3**

Large-scale flow properties. The time-mean eastward jet penetration length  $L_p$  [km], the total volume transport  $Q$  [Sv], and the relative errors  $\delta$  for different values of the eddy-viscosity  $\nu$  [ $\text{m}^2 \text{ s}^{-1}$ ] in the 3L, 6L and 12L solutions.

$\nu$	$L_p^{(3)}$	$L_p^{(6)}$	$L_p^{(12)}$	$Q^{(3)}$	$Q^{(6)}$	$Q^{(12)}$	$\delta(\bar{\psi}_1^{(3)}, \bar{\psi}_1^{(6)})$	$\delta(\bar{\psi}_1^{(6)}, \bar{\psi}_1^{(12)})$
100	2370	1740	1755	103	90	91	0.61	0.05
50	2865	2360	2302	123	119	113	0.57	0.05

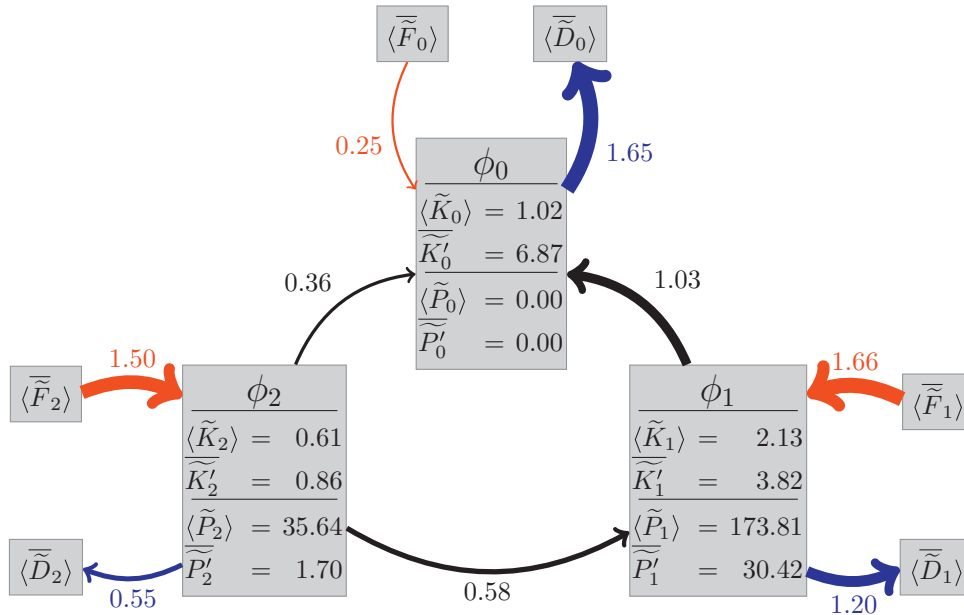


**Fig. 2.** Modewise energy diagram for the 3L solution at  $\nu = 100 \text{ m}^2 \text{ s}^{-1}$ ; only transfers of total energy are depicted in the diagram. The overbar and angle brackets denote the time and basin averages, respectively; and the prime stands for the fluctuating component of the quantity. Kinetic and potential energies of the  $i$ -th mode is denoted by  $\tilde{K}_i$  and  $\tilde{P}_i$ , while its forcing and dissipation by  $\tilde{F}_i$  and  $\tilde{D}_i$ , respectively. The size of the arrows is normalized to the maximum amplitude of the energy transfer, and the color indicates forcing (red) and dissipation (blue). (For interpretation of the references to colour in this figure legend, the reader is referred to the web version of this article.)

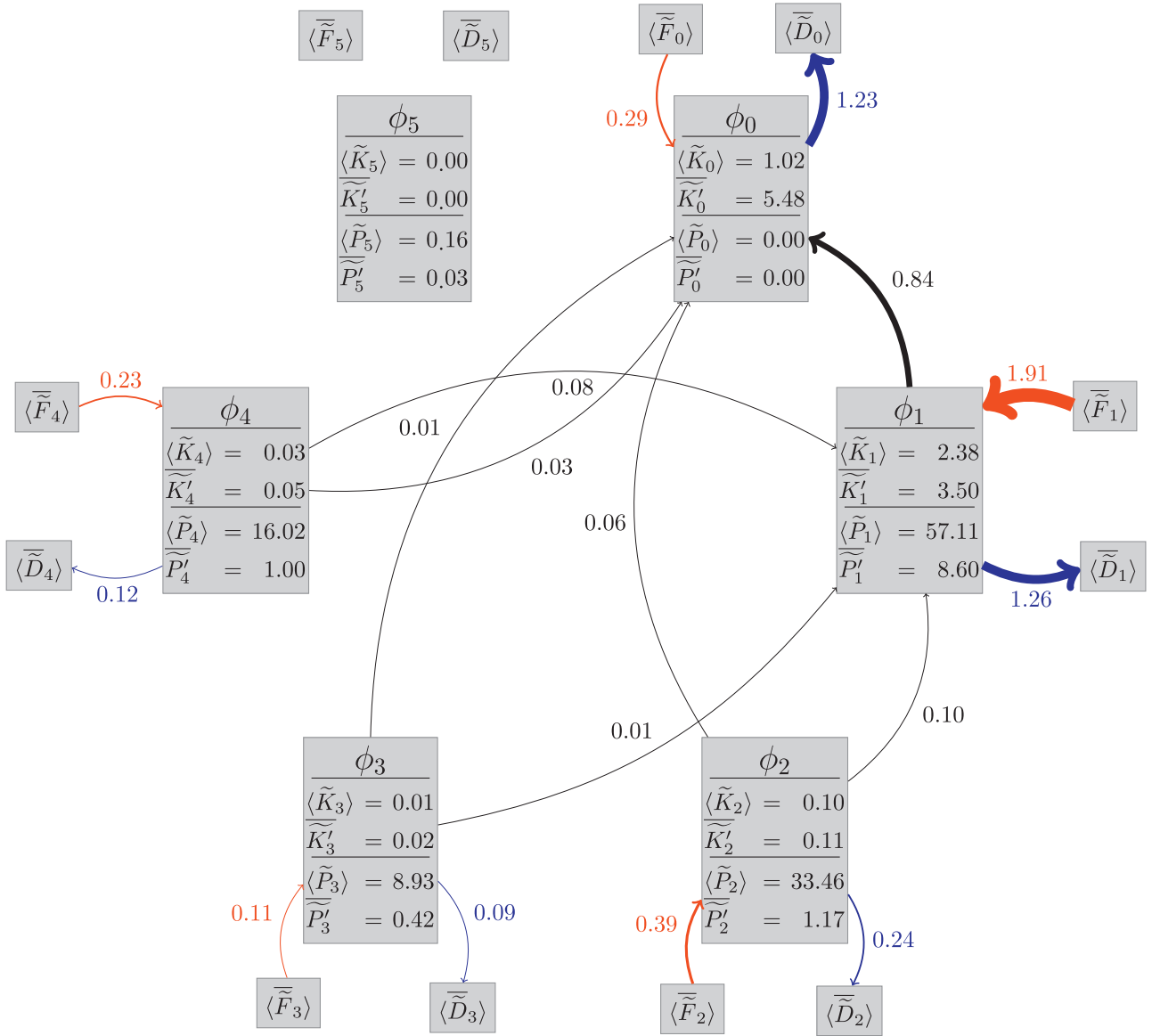


**Fig. 3.** Modewise energy diagram for the 6L solution at  $\nu = 100 \text{ m}^2 \text{ s}^{-1}$ ; only transfers of total energy are depicted in the diagram. Note that terms of order less than  $10^{-2}$  are not shown due to their negligible influence. The overbar and angle brackets denote the time and basin averages, respectively; and the prime stands for the fluctuating component of the quantity. Kinetic and potential energies of the  $i$ -th mode is denoted by  $\tilde{K}_i$  and  $\tilde{P}_i$ , while its forcing and dissipation by  $\tilde{F}_i$  and  $\tilde{D}_i$ , respectively. The size of the arrows is normalized to the maximum amplitude of the energy transfer, and the color indicates forcing (red) and dissipation (blue).

forcing  $\tilde{F}$  adds the forcing with the amplitude  $\tilde{f}_m$  only to the  $m$ -th mode, thereby altering its energy intake.

We introduced  $\hat{\mathbf{e}}_m$  as the standard unit basis vector (a vector of zeros with one at the position  $m$ ) and  $\tilde{f}$  as the forcing amplitude, and carried out a series of numerical experiments for  $\mathbf{f} = \tilde{f} \hat{\mathbf{e}}_m$ , with the goal to understand how the extra forcing of individual modes influences the eastward jet characteristics and the energy of flow fluctuations  $\tilde{E}$ .

In the 3L case, relatively moderate forcing  $\tilde{F}$  of  $\phi_0$ ,  $\phi_2$  (we applied up to 10% of the full reference wind stress with  $\tau_0 = 0.3 \text{ N m}^{-2}$ , rather than of the corresponding wind forcing component projected on the forced mode) results in 5% increase of the eastward jet length, while the same forcing being applied to  $\phi_1$  elongates the jet by 10%. Further increase of the forcing of  $\phi_0$ ,  $\phi_2$  leads to no changes in the jet length, while the jet does become longer by 15%, if only  $\phi_1$  is forced (Table 4). In the 6L case, the eastward jet length  $L_p^{(6)}$  always increases as the modes  $\phi_0$ ,  $\phi_1$  are forced, whereas for  $\phi_2$  this increase takes place up to only 10% of

the forcing, and then  $L_p^{(6)}$  decreases (Table 5). Forcing of the higher baroclinic modes  $\phi_m$  ( $m = 3, 4, 5$ ) up to the 10% of the initial forcing only slightly increases  $L_p^{(6)}$ , which remains nearly constant for the stronger forcing. Thus, we conclude that the higher baroclinic modes have much weaker effect on the eastward jet, and  $\phi_1$  is the most efficient mode in the eddy backscatter, however a deeper analysis addressing the physical mechanism making  $\phi_1$  the most efficient mode is beyond the scope of this paper.

Analysing the modewise energetics, we found that the higher is the intensity of the modewise forcing  $\tilde{F}$ , the larger are the modal energies of the mean flow and fluctuations, and that the energy inequality

$$\overline{\tilde{E}'_1} > \overline{\tilde{E}'_2} > \overline{\tilde{E}'_0}$$

as well as its analogue normalized to the total layerwise energy

$$\overline{\tilde{E}_1} > \overline{\tilde{E}_2} > \overline{\tilde{E}_0}$$

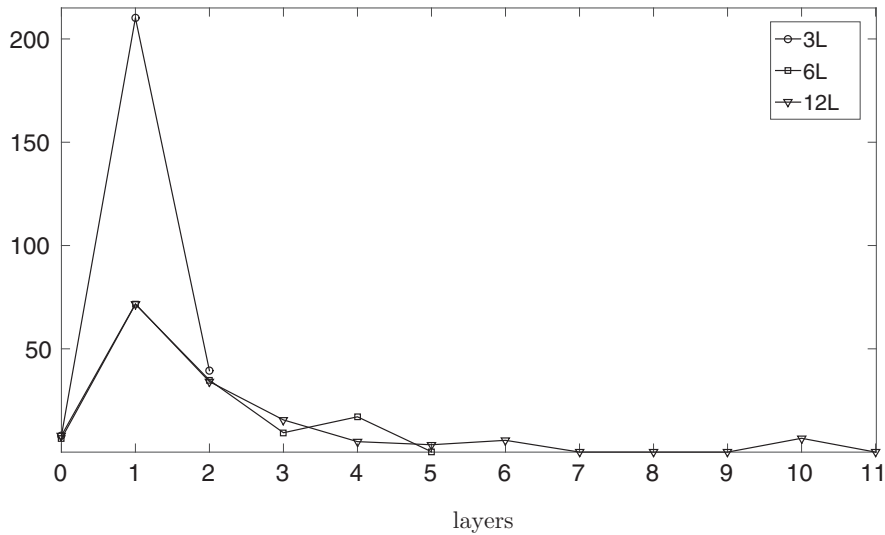


**Fig. 4.** Typical behaviour of the total modewise energy  $\tilde{E}$  of the 3L, 6L and 12L solutions normalized to its total layer-wise energy  $\bar{E}$  (the total energy integrated over all the layers) for  $\nu = 100 \text{ m}^2 \text{ s}^{-1}$  and the wind forcing  $\tilde{F}_w$ . Note that the inequality  $\tilde{E}_1 > \tilde{E}_2 > \tilde{E}_0$  holds true for all solutions thus making the first three modes players of fundamental importance in setting the behaviour the eastward jet extension of the western boundary currents. (For interpretation of the references to colour in this figure legend, the reader is referred to the web version of this article.)

**Table 4**

Efficiency of 3L modes. Effect of the mode-wise forcing  $\tilde{\mathbf{f}} = \tilde{f}_m \hat{\mathbf{e}}_m$ ,  $0 \leq m \leq 2$  on the eastward jet penetration length  $L_p^{(3)}$  and volume transport  $Q^{(3)}$ , in the 3L solution at  $\nu = 100 \text{ m}^2 \text{ s}^{-1}$ . Note that the  $L_p^{(3)} = 2370 \text{ km}$  and  $Q^{(3)} = 102.60 \text{ Sv}$  for  $\tilde{\mathbf{f}} = 0$ .

$m$ -th mode	$\tilde{f}_m$	$L_p^{(3)}$ [km]	$Q^{(3)}$ [Sv]
0	0.1	2500	107
1	0.1	2600	104
2	0.1	2500	96
0	0.2	2500	103
1	0.2	2650	119
2	0.2	2500	112
0	0.4	2500	118
1	0.4	2750	128
2	0.4	2500	102

**Table 5**

Efficiency of 6L modes. Effect of the mode-wise forcing  $\tilde{\mathbf{f}} = \tilde{f}_m \hat{\mathbf{e}}_m$ ,  $0 \leq m \leq 5$  on the eastward jet penetration length  $L_p^{(6)}$  and volume transport  $Q^{(6)}$ , in the 6L solution at  $\nu = 100 \text{ m}^2 \text{ s}^{-1}$ . Note that the  $L_p^{(6)} = 1740 \text{ km}$  and  $Q^{(6)} = 90.06 \text{ Sv}$  for  $\tilde{\mathbf{f}} = 0$ .

$m$ -th mode	$\tilde{f}_m$	$L_p^{(6)}$ [km]	$Q^{(6)}$ [Sv]
0	0.1	1800	91
1	0.1	1900	94
2	0.1	1800	85
3	0.1	1700	87
4	0.1	1750	86
5	0.1	1750	83
0	0.2	1800	90
1	0.2	2000	113
2	0.2	1450	81
3	0.2	1600	85
4	0.2	1700	84
5	0.2	1750	88
0	0.4	1950	104
1	0.4	2200	130
2	0.4	1500	80
3	0.4	1750	94
4	0.4	1700	82
5	0.4	1800	83

hold true for both 3L, 6L and 12L solutions (Fig. 4), and for all values of  $\tilde{F}$  studied. This also confirms the dominant role of the low modes  $\phi_0$ ,  $\phi_1$  and  $\phi_2$  in the eastward jet maintaining the eddy backscatter. The higher baroclinic modes are less energetic, their intermodal energy transfer rates are much lower compared to the lower modes, and their influences on the eastward jet length and volume transport are progressively weaker. Although, the higher baroclinic modes have a smaller effect, they still play an important special role (discussed below) in maintaining the eastward jet.

To study how the higher baroclinic modes affect the eastward jet, we damped them one by one and observed how this influences the flow dynamics. As an illustration of our approach, let us consider the highest 6L baroclinic mode  $\phi_5$ , which is seemingly negligible in the energy diagram, as we can judge from both its energy and intermodal energy transfers (Fig. 3), and filter it out from the solution by a strong mode-selective damping. Surprisingly, the suppression of this low-energy mode causes significant changes in the large-scale solution:  $L_p^{(6)}$  increases by 3.5%, and  $Q^{(6)}$  increases by 6.7%, and most of the resulting flow anomaly is induced in the first baroclinic mode. These changes may seem small, but if we take into account the minuscule intermodal energy transfer (of order  $10^{-8}$  to  $10^{-4}$ , non-dimensional units), the induced changes are relatively large. When we damped the more energetic mode  $\phi_3$ , the consequences were even more pronounced:  $L_p^{(6)}$  and  $Q^{(6)}$  decreased by 18% and 5%, respectively. All this leads us to the important conclusion that although the higher baroclinic modes cannot significantly elongate the eastward jet in isolation from the other modes, they are actively involved in the intermodal energy transfer that influences the jet indirectly. We studied this phenomenon further, by analysing the energy transfer terms between different modes, and found that the disproportion between the small amounts of energy transferred from the higher baroclinic modes to the lower modes and its relatively large effect on the eastward jet is explained by the fact that all this energy is injected locally into the neighborhood of the eastward jet. The energy injection region coincides with the region of the most intensive eddy forcing (Shevchenko and Berloff, 2015) that drives the eddy backscatter maintaining the eastward jet. The injections themselves can be viewed as parts of the inverse and spatially local energy cascade from high baroclinic to the first baroclinic and barotropic modes, which are the most efficient for the eddy backscatter.

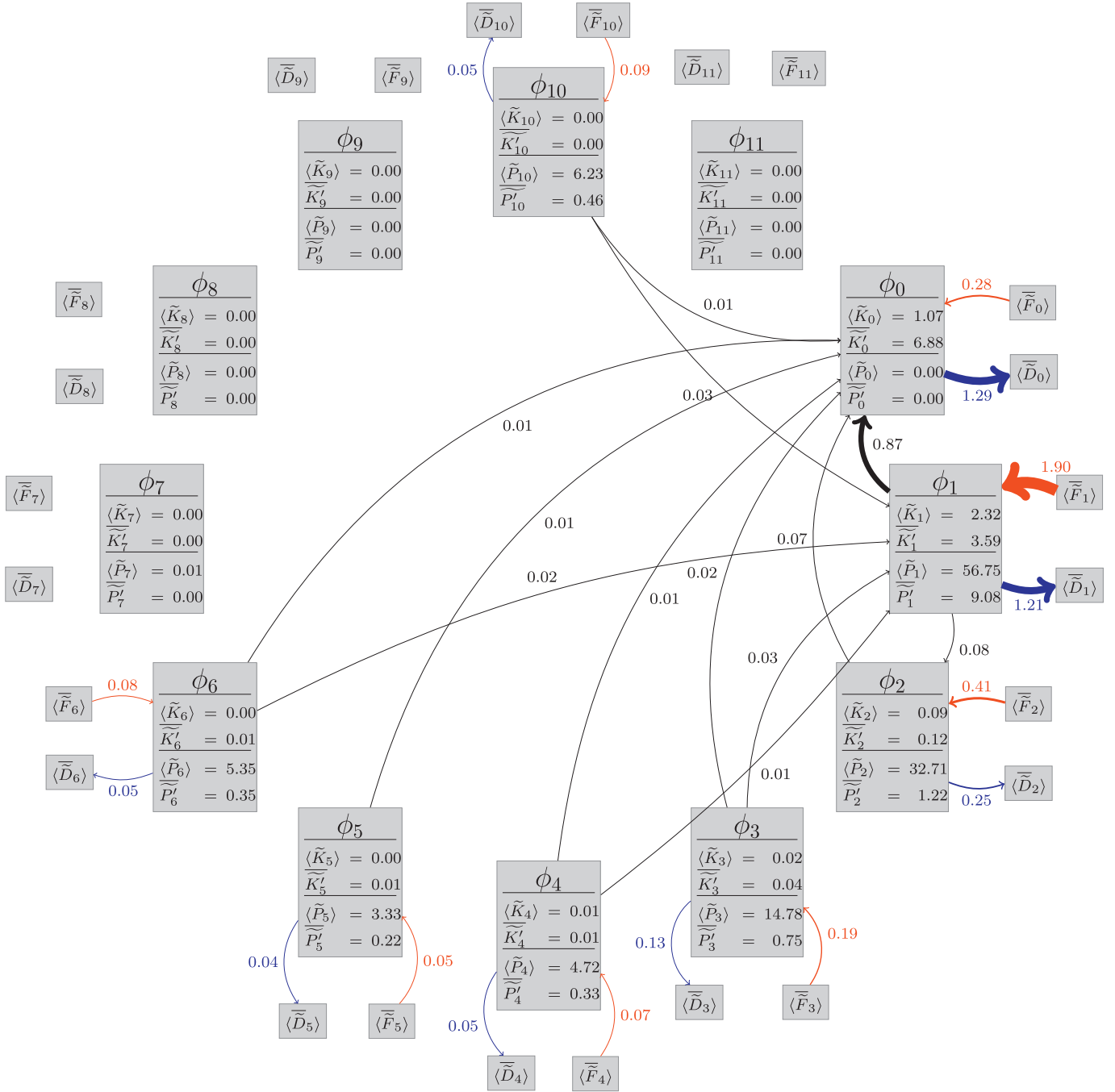


**Fig. 5.** Modewise energy diagram for the 12L solution at  $\nu = 100 \text{ m}^2 \text{ s}^{-1}$ ; only transfers of total energy are depicted in the diagram. Note that terms of order less than  $10^{-2}$  are not shown due to their negligible influence. The overbar and angle brackets denote the time and basin averages, respectively; and the prime stands for the fluctuating component of the quantity. Kinetic and potential energies of the  $i$ -th mode is denoted by  $\tilde{K}_i$  and  $\tilde{P}_i$ , while its forcing and dissipation by  $\tilde{F}_i$  and  $\tilde{D}_i$ , respectively. The size of the arrows is normalized to the maximum amplitude of the energy transfer, and the color indicates forcing (red) and dissipation (blue). (For interpretation of the references to colour in this figure legend, the reader is referred to the web version of this article.)

In order to better understand how even higher than  $\phi_5$  baroclinic modes influence the flow dynamics for  $\nu = 100 \text{ m}^2 \text{ s}^{-1}$  we computed the 12L model solution. From its analysis we found that the dynamics produces not only familiar upscale energy transfers (from higher to lower modes), as in the 6L case, but also some downscale transfers (from lower to higher modes, namely  $\phi_1 \rightarrow \phi_2$ ; Fig. 5); understanding significance and mechanisms of these forward energy transfers (the energy flow from larger to smaller scales (Vallis, 2006)) is beyond the scope of this paper. However, the overall effect of the baroclinic modes  $\phi_i, i = 6, 11$  on the

eastward jet is much smaller compared to the 6L high baroclinic modes, namely both  $L_p^{(12)}$  and  $Q^{(12)}$  differ from the 6L case by around 1%. Although, the modes in the 12L solution are more energetic, and the intermodal energy transfers are more intense than in the 6L case (Fig. 5). Thus, we conclude that six isopycnal layers are enough to resolve vertically the essential geostrophically and hydrostatically balanced double-gyre dynamics concentrated in the main pycnocline.

Finally, we studied how the eddy viscosity  $\nu$  affects the modewise energetics. We found that the outcome for the twice smaller

$\nu = 50 \text{ m}^2 \text{ s}^{-1}$  is qualitatively similar, but the flow and intermodal energy transfers are more energetic. Besides, we compared the 6L and 12L solutions at  $\nu = 50 \text{ m}^2 \text{ s}^{-1}$  and found that in the 12L case the volume transport is 5% larger. This is expected result, since both eddy energy and diverging eddy fluxes keep growing with decreasing  $\nu$ , without signs of saturation, and this growth is even steeper with higher vertical resolution and lower viscosity (Shevchenko and Berloff, 2015), suggesting more active roles of the highest modes.

Summarizing the findings of this section, we conclude that as the eddy viscosity decreases, both the energy of individual modes and the intermodal energy transfers increase. The bulk of energy drains from higher modes into the barotropic mode and the first baroclinic mode. From the latter it is also transferred down to the barotropic mode, thus making it the main recipient of the energy, followed by the first and second baroclinic modes. These findings are partly consistent with the conclusion of Smith and Vallis (2001; 2002), who argued that in horizontally homogeneous, eddy-resolving QG dynamics, the energy is transferred through the first baroclinic mode to the barotropic mode. Our results not only confirm this in more comprehensive model but also show that direct high-baroclinic-to-barotropic transfers are also possible. The energy exchange with the higher than  $\phi_5$  baroclinic modes is relatively minuscule, thus, supporting our previous conclusion that using more than six modes is not necessary for capturing the essential eddy effects in the double gyres.

#### 4. Conclusions and discussion

The goal of this study was to understand how the vertical baroclinic modes affect the eddy-resolving dynamics of the ocean gyres including the eastward jet extension of the western boundary currents, such as the Gulf Stream or Kuroshio, and their adjacent recirculation zones. Analyzing the difference between three- (3L) and six-layer (6L) solutions of the multi-layer quasi-geostrophic (QG) model of the wind-driven ocean gyres, we arrived at the conclusion that the higher baroclinic modes have an overall *inhibitory* effect on the eastward jet that is also in agreement with the conclusions in Shevchenko and Berloff (2015). This is opposite to what has been thought over the last 25 years since (Barnier et al., 1991). The main reason for the difference between our results and the ones reported in Barnier et al. (1991) is that the solutions in Barnier et al. (1991) were both symmetrically forced and underresolved. The former effect makes the eastward jet unrealistically long and strong, whereas the effect of the latter is opposite; the outcome was misleading, as we found (our solutions repeating the results of Barnier et al. (1991) are not shown for brevity).

We found that in the absence of high baroclinic modes, the energy input from the wind is more efficiently focused onto the lower modes, therefore, the eddy backscatter is stronger, and amplification of the eastward jet is dominated by the first baroclinic mode. However, the higher baroclinic modes still play an important role by transferring energy to the lower modes locally, directly into the most active eddy backscatter region around the eastward jet. The overall effect of the high baroclinic modes upon the eastward jet is such that the higher than the fifth baroclinic modes play negligible roles, hence, keeping only six isopycnal layers should be enough to resolve the mesoscale eddy dynamics and backscatter in the ocean gyres. This conclusion are pertinent to the explored range of eddy viscosity values, and further analyses at much lower viscosities remain to be carried out.

Our conclusions are consistent with those of Smith and Vallis (2001, 2002), who studied horizontally homogeneous, eddy-resolving QG dynamics. More specifically, in Smith and Vallis (2001, 2002) it has been found that the energy in high baroclinic modes (higher than the first one) is transferred to the barotropic

mode through the first baroclinic mode. This finding is partially confirmed in our work. We found that both the energy in the high baroclinic modes does transfer to the barotropic mode, but not necessarily through the first baroclinic mode, as there are also direct transfers. Another finding is that the 12L model exhibits both forward and backward energy cascades, although the latter substantially prevails.

We have also studied how decrease in the eddy viscosity is reflected in the modewise energetics and found that the modes and the eddy backscatter in less viscous flows become more energetic, but the overall eddy effects remain qualitatively similar. We conclude that although the 3L QG model captures the essential eddy dynamics, it significantly overestimates the backscatter (with respect to the 6L and 12L cases) and the higher baroclinic modes are required for a quantitatively accurate representation of the eddy effects.

Further extensions of our results can focus on more realistic primitive-equation models of the North Atlantic, and on the deeper understanding of the eddy backscatter. On the other hand, successful application of the multi-modal energetics analysis in the QG context suggests its extension into primitive equations for similar dynamical analyses in comprehensive OGCMs.

#### Acknowledgments

The authors are thankful to the [Natural Environment Research Council](#) for the support of this work through the grant [NE/J006602/1](#) and the use of ARCHER (the UK National Supercomputing Service). We express our gratitude to Simon Burbidge and Matt Harvey for their help with Imperial College London cluster, as well as to Andrew Thomas for his help with managing and maintaining the data storage. The authors would also like to thank unknown referees for valuable comments and suggestions, which helped us greatly improve our work.

#### References

- Barnier, B., Provost, C.L., Hua, B.L., 1991. On the catalytic role of high baroclinic modes in eddy-driven large-scale circulations. *J. Phys. Oceanogr.* 21 (7), 976–997.
- Berloff, P., 2005a. On dynamically consistent eddy fluxes. *Dynam. Atmos. Ocean.* 38 (3–4), 123–146.
- Berloff, P., Hogg, A., Dewar, W., 2007. The turbulent oscillator: a mechanism of low-frequency variability of the wind-driven ocean gyres. *J. Phys. Oceanogr.* 37 (9), 2363–2386.
- Berloff, P., McWilliams, J., 1999a. Large-scale, low-frequency variability in wind-driven ocean gyres. *J. Phys. Oceanogr.* 29 (8), 1925–1949.
- Berloff, P., McWilliams, J., 1999b. Quasigeostrophic dynamics of the western boundary current. *J. Phys. Oceanogr.* 29 (10), 2607–2634.
- Dijkstra, H., Ghil, M., 2005. Low-frequency variability of the large-scale ocean circulation: a dynamical systems approach. *Rev. Geophys.* 43 (3), 1–38.
- Gula, J., Molemaker, M.J., McWilliams, J.C., 2015. Gulf stream dynamics along the southeastern u.s. seaboard. *J. Phys. Oceanogr.* 45 (3), 690–715.
- Hogg, A., Dewar, W., Berloff, P., Kravtsov, S., Hutchinson, D., 2009. The effects of mesoscale ocean-atmosphere coupling on the large-scale ocean circulation. *J. Climate.* 22 (15), 4066–4082.
- Karabasov, S.A., Berloff, P.S., Goloviznin, V.M., 2009. CABARET In the ocean gyres. *Ocean Model.* 30 (2–3), 155–168.
- Kirtman, B., Bitz, C., Bryan, F., Collins, W., Dennis, J., Hearn, N., Kinter III, J., Loft, R., Rousset, C., Siqueira, L., Stan, C., Tomas, R., Vertenstein, M., 2012. Impact of ocean model resolution on CCSM climate simulations. *Clim. Dyn.* 39 (6), 1303–1328.
- Marsh, R., A. de Cuevas, B., Coward, A.C., Jacquin, J., Hirschi, J.J.-M., Aksenov, Y., Nurser, A.J.G., Josey, S.A., 2009. Recent changes in the north atlantic circulation simulated with eddy-permitting and eddy-resolving ocean models. *Ocean Model.* 28 (4), 226–239.
- McWilliams, J.C., 1977. A note on a consistent quasigeostrophic model in a multiply connected domain. *Dynam. Atmos. Ocean.* 1 (5), 427–441.
- McWilliams, J.C., 2008. The Nature and Consequences of Oceanic Eddies. *Ocean Modeling in an Eddy Regime*, Vol. 177. Wiley.
- Pedlosky, J., 1987. *Geophysical fluid dynamics*. Springer-Verlag, New York.
- Sapsis, T., Dijkstra, H., 2013. Interaction of additive noise and nonlinear dynamics in the double-gyre wind-driven ocean circulation. *J. Phys. Oceanogr.* 43 (2), 366–381.
- Shevchenko, I., Berloff, P., 2015. Multi-layer quasi-geostrophic ocean dynamics in eddy-resolving regimes. *Ocean Model.* 94, 1–14.

- Simonnet, E., Ghil, M., Dijkstra, H., 2005. Homoclinic bifurcations in the quasi-geostrophic double-gyre circulation. *J. Mar. Res.* 63 (5), 931–956.
- Smith, K., Vallis, G., 2001. The scales and equilibration of midocean eddies: freely evolving flow. *J. Phys. Oceanogr.* 31 (2), 554–571.
- Smith, K., Vallis, G., 2002. The scales and equilibration of midocean eddies: forced-dissipative flow. *J. Phys. Oceanogr.* 32 (6), 1699–1720.
- Treguier, A.M., Deshayes, J., Le Sommer, J., Lique, C., Madec, G., Penduff, T., Molines, J.-M., Barnier, B., Bourdalle-Badie, R., Talandier, C., 2014. Meridional transport of salt in the global ocean from an eddy-resolving model. *Ocean Sci.* 10, 243–255.
- Vallis, G.K., 2006. *Atmospheric and oceanic fluid dynamics: Fundamentals and large-scale circulation*. Cambridge University Press, Cambridge, UK.
- Wunsch, C., 1997. The vertical partition of oceanic horizontal kinetic energy. *J. Phys. Oceanogr.* 27 (8), 1770–1794.